www.elsevier.com/locate/jbiomech

the Influence of anesthesia and fluid-structure interaction on simulated shear stress patterns in the carotid bifurcation of mice

David De Wilde, Bram Trachet, Guido De Meyer, Patrick Segers

PII: S0021-9290(16)30670-4
DOI: http://dx.doi.org/10.1016/j.jbiomech.2016.06.010
Reference: BM7764

To appear in: *Journal of Biomechanics*

Received date: 2 March 2016
Revised date: 4 May 2016
Accepted date: 7 June 2016

Cite this article as: David De Wilde, Bram Trachet, Guido De Meyer and Patricl Segers, the Influence of anesthesia and fluid-structure interaction on simulate shear stress patterns in the carotid bifurcation of mice, *Journal of Biomechanics* http://dx.doi.org/10.1016/j.jbiomech.2016.06.010

THE INFLUENCE OF ANESTHESIA AND FLUID-STRUCTURE INTERACTION ON SIMULATED SHEAR STRESS PATTERNS IN THE CAROTID BIFURCATION OF MICE

David De Wilde[1], Bram Trachet[1,2], Guido De Meyer[3], Patrick Segers[1]

[1] IBiTech-bioMMeda, Ghent University-IMinds Medical IT, Ghent, Belgium

[2] Department of Bioengineering, EPFL, Lausanne, Switzerland

[3] Division of Physiopharmacology, University of Antwerp, Antwerp, Belgium

Keywords: Carotid bifurcation, Mice, Wall shear stress, Computational Fluid Dynamics, Fluid-Structure Interaction.

Correspondence to:

Bram Trachet

bioMMeda, De Pintelaan185-blokB5, B-9000 Gent, Belgium

Tel: + 32 (0)9 332 46 21

Fax: +32(0) 93324159

Email: Bram.Trachet@ugent.be

Word Count: 3965

ABSTRACT

Background: Low and oscillatory wall shear stresses (WSS) near aortic bifurcations have been linked to the onset of atherosclerosis. In previous work, we calculated detailed WSS patterns in the carotid bifurcation of mice using a Fluid-Structure Interaction (FSI) approach. We subsequently fed the animals a high-fat diet and linked the results of the FSI simulations to those of atherosclerotic plaque location on a within-subject basis. However, these simulations were based on boundary conditions measured under anesthesia, while active mice might experience different hemodynamics. Moreover, the FSI technique for mouse-specific simulations is both time- and labour-intensive, and might be replaced by simpler and easier Computational Fluid Dynamics (CFD) simulations. The goal of the current work was (i) to compare WSS patterns based on anesthesia conditions to those representing active resting and exercising conditions; and (ii) to compare WSS patterns based on FSI simulations to those based on steady-state and transient CFD simulations. **Methods:** For each of the 3 computational techniques (steady state CFD, transient CFD, FSI) we performed 5 simulations: 1 for anesthesia, 2 for conscious resting conditions and 2 more for conscious active conditions. The inflow, pressure and heart rate were scaled according to representative in vivo measurements obtained from literature. **Results:** When normalized by the maximal shear stress value, shear stress patterns were similar for the 3 computational techniques. For all activity levels, steady state CFD led to an overestimation of WSS values, while FSI simulations yielded a clear increase in WSS reversal at the outer side of the sinus of the external carotid artery that was not visible in transient CFD-simulations. Furthermore, the FSI simulations in the highest locomotor activity state showed a flow recirculation zone in the external carotid artery that was not present under anesthesia. This recirculation went hand in hand with locally increased WSS reversal. **Conclusion(s):** Our data show that FSI simulations are not necessary to obtain normalized

WSS patterns, but indispensable to assess the oscillatory behavior of the WSS in mice. Flow recirculation and WSS reversal at the external carotid artery may occur during high locomotor activity while they are not present under anesthesia. These phenomena might thus influence plaque formation to a larger extent than what was previously assumed.

INTRODUCTION

The hypothesis that low and oscillatory wall shear stress (WSS) has an atheroprone effect on the endothelial cells lining the inner arterial wall is generally accepted (Asakura and Karino, 1990; Chatzizisis et al., 2007; Ku et al., 1985; Peiffer et al., 2013b). In mouse models of atherosclerosis, it has been shown that atherosclerotic lesions preferentially develop at branching points, bifurcations and at the bends of arteries (Nakashima et al., 1994). To be able to determine murine WSS directly, highly accurate and therefore challenging measurements of the blood velocity near the arterial wall would be needed. A commonly used alternative are computer simulations that derive the WSS from the spatial velocity gradient perpendicular to the arterial wall. The simplest type of numerical simulations to calculate WSS in arteries are steady state CFD calculations. In these calculations either the peak or mean velocity (or flow) is applied at the boundaries and the temporal variability is ignored. Transient CFD simulations take into account the time-dependency of the blood flow. In this case the time-averaged WSS (TAWSS) is used to quantify the shear stress patterns while the Oscillatory Shear Index (OSI) quantifies its oscillatory behavior, which is assumed to play an important role in the atheroprone effect of shear stresses on the endothelium. A final step is the inclusion of the mechanical behavior of the arterial wall into the model, resulting in FSI simulations that take both the hemodynamics and the buffering effect of the arteries into account. This adds an extra layer of complexity to the modelling methodology, but also results in more realistic simulations.

Computer simulations of the mouse vasculature have already been performed by many authors. Most of these publications focused on the methodology and the feasibility to calculate WSS in mice and did not link the found patterns (quantitatively or qualitatively) to biological responses or processes (Feintuch et al., 2007; Greve et al., 2006; Huo et al., 2008; Trachet et al., 2011a; Trachet et al., 2009; Van Doormaal et al., 2014). Nevertheless steady state CFD WSS patterns in the common carotid artery have been linked to the uptake of plasma macromolecules (Mohri et al., 2014) or local wall thickness (Cheng et al., 2004). Transient CFD simulations have been used to link TAWSS and OSI patterns to aneurysm progression on a within-subject basis (Ford et al., 2011; Trachet et al., 2011b). In the carotid artery, transient CFD has been used to link wall shear stress patterns with plaque development (Assemat et al., 2014). In order to get access to the pre-disease geometry, the authors virtually removed the plaque from the model. Other studies linked wall shear metrics from transient CFD with plaque progression markers such as presence of fat in the wall (Suo et al., 2007) or the expression of VCAM-1 (Hoi et al., 2011). In these studies, the CFD simulations were performed in another group of animals than the group that was used to determine the progression marker(s). Recently we have published a study presenting the first mouse-specific FSI simulations in the murine carotid bifurcation (De Wilde et al., 2015a), and we subsequently linked the shear stress patterns to plaque formation on a within-subject basis (De Wilde et al., 2015b).

When interpreting data from computer simulations in mice it is important to keep in mind that the used computational technique may influence the outcome of the simulations. When comparing steady state and transient CFD in the mouse aortic arch only a small difference in absolute value of TAWSS was found (Feintuch et al., 2007). However, the effect of FSI on wall shear stress computations in mice has, to the best of our knowledge, never been investigated. Moreover, the boundary conditions used for these simulations are based on measurements obtained while the mice were under anesthesia. Anesthesia lowers the mean arterial pressure

(MAP), the cardiac output and the heart rate (Janssen et al., 2004; Komarek, 2007). When the activity level of a mouse increases, these parameters will increase correspondingly. This can considerably influence the simulated flow patterns (Mohri et al., 2014). Intrigued by these results, we performed a parameter study in which we investigated not only the influence of different simulation techniques (steady state CFD, transient CFD, FSI) but also the influence of anesthesia and locomotor activity on simulated wall shear stress patterns in the carotid bifurcation of the mouse.

MATERIAL AND METHODS

Experimental protocol

The study was based on data acquired in a female ApoE$^{-/-}$ mouse that was fed a Western type diet (TD88137, Harlan Teklad, USA) ad libitum from the age of 6 weeks until 16 weeks. The housing of the animal and all the experiments were the same as in our previous publications (De Wilde et al., 2015a; De Wilde et al., 2015b). All experiments were approved by the animal ethics committee of Ghent University and conducted according to their guidelines. At week 16 the mouse underwent an imaging protocol. Using a high-frequency ultrasound scanner (Vevo 2100, Visual Sonics, Canada) with a linear array probe (MS550D, 22-55 MHz), the blood flow velocity was assessed in the common, external and internal carotid arteries of the left carotid bifurcation with Pulsed Wave Doppler. The distension of the artery was measured using M-mode. A contrast-enhanced (100 µl/25g body weight of Aurovist, Nanoprobes, USA) µCT scan (Triumph II, TriFoil Imaging, USA) provided the geometrical information of the carotid bifurcation at an isotropic resolution of 50 µm.

Post-processing of the measurements

The outer envelope of the Doppler signal and the diameter distension of the M-mode measurements were tracked to obtain respectively the blood velocity and the diameter curve. For the three locations (common, external (ECA) and internal (ICA) carotid artery) both signals were aligned in time. In order to calculate the instantaneous average velocity over the cross-section, the maximum velocity was divided by 2 assuming a parabolic flow profile at the measurement location (which was confirmed a posteriori by the simulations). Due to measurement errors and assumptions in the data processing, the time-averaged mass flow balance in the model (cycle-averaged difference between in- and outflow) was not completely fulfilled. As we estimated the CCA measurement to be the most accurate, a scaling factor c=1.1275 was applied to the ICA and ECA mass flows such that the measured mass flow at the CCA was equal to the sum of the measured mass flows at ICA and ECA, multiplied with c. Mimics (Materialise, Leuven, Belgium) was used to semi-automatically segment the three branches of the carotid bifurcation from the μCT datasets. Flow extensions with a length equal to the diameter of the arteries were added in VMTK (www.vmtk.org). Finally, the segmented geometry was shrunk to the diastolic radius as measured with M-mode, resulting in a geometrical shrinking factor of 0.84. From the resulting STL-surface, a volume mesh of both the fluid (lumen) and the solid (arterial wall) domain was constructed using the in-house developed XTM meshing method (Bols et al., 2016). A mesh convergence study resulted in convergence for 300k fluid domain cells and 65k solid domain cells (De Wilde et al., 2015a). The wall thickness of the artery was assumed to be 10% of the local luminal diameter.

Steady state CFD simulations

For the steady state CFD simulations 2 sets of BCs were applied: (i) the average velocity/flow of the three branches and (ii) the peak velocity of the three branches. For both cases, the mass-

flow of the three branches was calculated as described above. At the common carotid the calculated mass flow was applied. At the external and internal carotids the mass flow split was calculated and they were imposed as outflow boundary conditions with a constant outflow fraction. For the steady state simulations convergence was reached when the continuity and momentum residuals dropped below $1e^{-10}$.

Transient CFD simulations

For the transient CFD simulations a mass flow inlet was applied at both the common and external carotid (at the external carotid the mass flow inlet behaved as an outflow). The internal carotid was modelled as a traction free outlet. For the transient CFD simulations a convergence criterion of $1e^{-10}$ was applied for both the continuity and the momentum equations.

Transient FSI simulations

The methodology for the FSI simulations is described in depth in our previously published work (De Wilde et al., 2015a). In short, the same mass flow inlets as for transient CFD simulations were applied. At the ICA a 3-element windkessel model was implemented, with parameters fitted to the mouse-specific ultrasound measurements. The external tissue support was modelled using linear springs. The backward incremental method was executed sequentially to take axial and diastolic pre-stresses into account (De Wilde et al., 2015a). The absolute coupling iterations convergence criteria for the residuals were set to 10^{-8} m for the displacement and 0.5 Pa for the load at the interface.

Influence of locomotor activity

During a period of high locomotor activity (=active state), the hemodynamic parameters increase even further than in the conscious resting case. The reported increase is: heart rate + 23.77%, blood flow +93% and blood pressure +31.3% (Janssen et al., 2004). This extra in-

crease rescaled case *Rest1* to case *Active1*, the lower bound estimate of the active condition. Similarly, *Active2* was defined as the adaptation of case *Rest2* with regard to the influence of locomotor activity (Table 1). In both active cases the heart rate, blood flow and blood pressure are increased substantially. Once again, the change in heart rate could only be applied to the transient simulations (transient CFD and FSI) and the blood pressure only for the FSI simulations. For the CFD simulations, the boundary conditions were simply scaled according to the rescaling factors of Table 1. For the FSI simulations the first step was to recalculate the 3-element windkessel model terminating the ICA based on the new, rescaled flow and blood pressure. It is important to note that the rescaled pressure was not applied explicitly, but implicitly through this windkessel approach. For both the common and external carotids the rescaled mass flows were applied at the boundaries. The pre-stress calculation was not repeated, because the previously found diastolic stress-state (at a pressure of 87 mmHg) was still valid.

Post-processing of simulated data

WSS was calculated for steady-state CFD simulations, and TAWSS for transient CFD and FSI simulations. WSS and TAWSS were normalized by their mean value to allow for a comparison of patterns rather than values. For transient simulations the OSI was calculated as well (already dimensionless). The influence of anesthesia was visualized by the diastolic state of FSI simulations. In order to visualize the presence of recirculation structures, the line integral convolution (LIC) of the normalized WSS was plotted in the early deceleration phase. The LIC is the mathematical equivalent on a surface of putting drops of ink in a flow/vector field and was calculated for FSI simulations at different activity levels. Finally, the area experiencing reversed WSS was calculated for each computational technique and for each boundary condition. Reversed WSS was quantified using the scalar product of the WSS with the normal of the CCA inlet boundary. If the scalar product was negative (component in the direction of

the CCA), the zone was indicated to have a reversed WSS. For the transient simulations the calculation of reversed WSS was done in the early deceleration phase. This definition of reversed WSS was not applicable when the WSS vector was perpendicular to the inlet normal, which was the case at the stagnation point of the bifurcation.

Statistics

In order to compare different simulation techniques and activity levels we adopted a statistical technique analysis that has been described in detail in our previous work (De Wilde et al., 2015b). Briefly, we applied the surrogate sample data analysis (Peiffer et al., 2013a) to study correlations between the calculated hemodynamic wall parameters obtained from different simulations. The similarity of the distribution of two different variables is described by Spearman's rank correlation coefficient ρ (Rowland et al., 2015) and Pearson`s correlation coefficient. The correlation is determined for the original values of the variables and for n_{sur} scrambled distributions of one of the variables (=surrogates). The statistical test ascertains that the original correlation coefficient is higher than the 95% percentile of the random distributions (i.e. the right-hand side of the histogram – right tailed test). To take into account the spatial autocorrelation of the variables, extra sampling steps (n_{smp}) were performed. The sample size s_{smp} was calculated using: $s_{smp} = s_{map}/l_{dec}^2$. In this formula s_{map} was the original number of grid points (s_{map}=29501) and l_{dec} the spatial de-correlation length (l_{dec}=20), which resulted in a conservative value of s_{smp}= 74 (De Wilde et al., 2015b). The final histogram was averaged over n_{smp} histograms (one for each sampling step) and an error tolerance of 10^{-4} was used for the p-value, which resulted in a minimal value of n_{sur}=500 and n_{smp}=500. The found (positive) correlation was considered to be significant (indicated with *) if both $p<0.05$ and $LCB_{p=0.05} > 0$, and highly significant (indicated with **) if both $p<0.001$ and $LCB_{p=0.001} > 0$. All statistics were done on a bifurcation level, combining the three branches into a single statistical test.

RESULTS

Comparison of computational techniques

The flow-split going to the internal and external carotid branches differed between the mean flow steady state CFD simulation (0.13/0.87) and the peak flow steady state CFD simulation (0.24/0.76). The transient CFD flow in the internal carotid (Figure 1a) was much more peaked compared to the corresponding transient FSI flow (Figure 1b): the FSI simulations approximated the measurements markedly better than the CFD simulations. The (TA)WSS calculated by all three CFD techniques (mean steady state CFD, transient CFD and transient CFD) reached a high and significant correlation ($r=0.99$, 0.96 and 0.99; $\rho=0.99$, 0.94 and 0.99 respectively) with the TAWSS calculated by FSI (Figure 2a). Nevertheless WSS was substantially higher when the peak velocity was used as a boundary condition for steady state CFD simulations (Figure 3a). After normalization by their mean values (3.25, 7.54, 3.42 and 2.85 Pa for mean CFD, peak CFD, transient CFD and FSI respectively) the WSS patterns showed very similar distributions for all techniques (Figure 3b). Nevertheless, the transient CFD simulations showed an important difference in oscillatory behavior when compared to FSI. The correlation was no longer significant and dropped to $r=0.03$ and $\rho=0.30$ (Figure 2b). In the transient CFD simulation the OSI was negligible with an average value of $1.3\ 10^{-3}$ and a maximum value of 0.166 (at the flow stagnation point, Figure 3c). For the FSI simulation on the other hand, there was a clear increase in OSI at the outer side of the ECA sinus, increasing the average value to $2.46\ 10^{-2}$ with a maximum value of 0.272. FSI simulations also resulted in a larger area experiencing reversed WSS (Figure 4d).

Influence of anesthesia and locomotor activity

For all 4 increased activity states (*Rest1, Rest2, Active1 and Active2)* the FSI-based TAWSS was highly and significantly correlated to the TAWSS calculated under anesthesia (Figure 2c, r=0.99, 0.99, 0.99, 0.97 and ρ=0.99, 0.99, 0.98, 0.98 respectively). The TAWSS increased with a rising activity level (Figure 4a), mainly due to the increase in flow. The normalized TAWSS distribution was, however, very similar for all simulated cases (Figure 4b). For *Anaesthesia, Rest1, Rest2, Active1 and Active2* the average TAWSS was 2.85, 3.08, 5.12, 4.77 and 8.11 Pa respectively. The most apparent difference between different states was the relatively high normalized TAWSS at the inner bend of the bifurcation. Unlike the normalized TAWSS, the OSI was markedly affected by an increase in activity level (Figure 2d). The correlation with the OSI calculated under anesthesia remained significant but the correlation coefficients decreased slightly for increasing activity levels (r=0.99, 0.97, 0.97, 0.86 and ρ=0.99, 0.98, 0.94, 0.91 respectively). Most of this discrepancy could be related to an increase in OSI near the ostium of the ECA with rising activity levels (Figure 4c). No difference in OSI was discernible in the CCA or the ICA. A detailed quantification of the surface area experiencing WSS reversal confirmed that reversed WSS occurs at the outer bend of the ECA sinus for cases *Rest2, Active1* and *Active2* (Figure 4d). Especially for the case *Active 2* a substantial zone with reversed WSS was observed. The LIC confirmed that flow recirculations were most apparent in the cases with highest locomotor activity (Figure 5a). For the FSI simulation of *Active2*, the most extreme case with high locomotor activity and the highest estimated influence of anesthesia, the LIC was calculated at different time points in the mid plane of the ECA (Figure 5b). This figure shows that the flow recirculation was maximal during the early deceleration phase (t_2), which was also the time point used for Figure 5a. These data are consistent with the elevated OSI (Figure 4c) and the locally increased WSS reversal (Figure

4d) that were both observed at the outer bend of the ECA for case *Active2*. Due to the presence of the flow recirculation the magnitude of the velocity vectors remained low at this location (Figure 5b).

DISCUSSION

Comparison of computational techniques

In this paper, several modelling strategies to simulate the murine carotid hemodynamics were compared. The focus of the comparison was on the WSS and other hemodynamic wall parameters. We found that the (normalized) WSS pattern was virtually the same for all the modelling strategies (Figure 2a, 3b), despite the clearly different boundary conditions that were applied (Figure 1a, 1b). Even the inclusion of the pulsatile nature of the blood flow (transient CFD and FSI) and/or the inclusion of the buffering capacity of the carotid artery (FSI) had little effect. Nonetheless, although the normalized WSS patterns were similar, the absolute values differed between CFD and FSI simulations because the total flow through the specific geometry was not constant and because the pulsatile pressure component led to a cyclic inflation of the arteries in the FSI simulations, which influenced the cross-sectional area (Figure 1c). A larger impact was found for parameters reflecting the oscillatory behavior of the WSS (Figure 2, 3c, 4d). The clearly higher oscillatory character of the ECA flow in the FSI simulations is directly related to the buffering capacity of the latter. Thanks to this buffering capacity FSI allowed for a net instantaneous flow imbalance and thus a net in/outflow difference, while the CFD simulations had to comply with an instantaneous mass balance at all times. Our data therefore suggest that in the carotid artery of mice FSI offers less restrictive simulation conditions, and may capture small oscillations that were not present in CFD.

Influence of anesthesia and locomotor activity

Decreased flow measurements due to anesthesia can have a big influence on the simulation results (Mohri et al., 2014). Confirming literature data, we also observed the presence of a flow recirculation at the outer sinus of the ECA when conscious conditions and locomotor activity were taken into account (Figure 4). As a result of the changed boundary conditions (Table 1) the peak systolic Reynolds number in the common carotid changed from 13.38 (*Anesthesia*) to 39.57 (*Active2*). For the same cases the Womersley number increased from 0.44 to 0.70. These data indicate that one should interpret the results of simulations that assume anesthesia with caution. Our normalized TAWSS patterns were rather robust with regard to different activity levels. However, absolute values of the WSS/TAWSS were heavily influenced by the precise boundary conditions and the level of locomotor activity. Therefore it makes sense for future work to report normalized WSS metrics rather than absolute values. Finally, the OSI (Figure 4c) and the reversed WSS (Figure 4d) showed a markedly different distribution depending on the physiological state. The location of the region with elevated OSI and reversed WSS was similar for all simulations, but the shape and size of this location was not, with the largest increase in the presence of extensive locomotor activity. Flow recirculation may thus develop in highly active mice while it is not present under anesthesia or conscious resting conditions.

Implications for the interpretation of previously published work

We believe that the largest impact of our findings lies in the (re-)interpretation of CFD simulations in mice. Many authors have tried to link local disease patterns to focal zones of locally disturbed shear stress using rigid-walled models of either the aortic arch (Assemat et al., 2014; Feintuch et al., 2007; Suo et al., 2007; Yap et al., 2014), the abdominal aorta (Ford et al., 2011; Greve et al., 2006; Trachet et al., 2011b; Willett et al., 2010) or both (Hoi et al., 2011;

Huo et al., 2008; Van Doormaal et al., 2014). The findings of publications that focused on regular WSS patterns (Feintuch et al., 2007; Greve et al., 2006; Huo et al., 2008; Suo et al., 2007; Willett et al., 2010; Yap et al., 2014) are not affected much by our results. However, some findings of publications that focused on the oscillatory patterns of WSS (Assemat et al., 2014; Ford et al., 2011; Hoi et al., 2011; Trachet et al., 2011b; Van Doormaal et al., 2014) might need to be re-interpreted. In this respect it is important to keep in mind that our results were obtained in the carotid artery, and our conclusions may therefore not be valid in other aspects of the aorta. The fact that most of the CFD simulations mentioned above were based on boundary conditions measured under anesthesia does not seem to compromise their findings too much. That also holds for publications that estimated shear stress patterns in the carotid artery from Doppler measurements under anesthesia. In their seminal paper from 2006, Cheng et al used this technique to demonstrate that atherosclerotic lesions developed invariably in the regions of the carotid artery where vortices and low shear stress had been induced by a perivascular shear stress modifier, whereas the regions in which the device induced an increased shear stress were protected from plaque development (Cheng et al., 2006). While a perivascular cast may induce more vortices in conscious mice than under anesthesia, our results do not affect their basic findings.

Limitations and future work

Our simulations are inherently limited by the spatial and temporal resolution of the preclinical imaging that provided the geometry and boundary conditions. But while future improvements in imaging might improve the level of details (e.g. small branches) that can be included (Trachet et al., 2015), we are confident that the main message of this paper will still be valid. It should be noted that our estimated increase in blood flow through the common carotid artery due to locomotor activity was probably on the high side and thus represents a worst case

scenario. At high locomotor activity, the cardiac output increases because of an increase in blood flow towards the skeletal muscles, while the main perfusion area of the carotid arteries is the brain (Marieb and Hoehn, 2008). In humans, the cerebral blood flow only peaks at the onset of physical activity and decreases again during constant physical activity, while the cardiac output is still at an elevated level (Querido and Sheel, 2012). The initial increase due to physical exercise (steady-state cycling) has been quantified for healthy humans as 27.9 ± 28.6% and the increase during prolonged exercise has been reported 2.6 ± 13.5% (Hiura et al., 2014). Both of these changes are smaller than the increase in cardiac output which is 92% and 118% respectively. It is thus likely that when mice are active the change in blood flow through the carotid arteries is smaller than the change in cardiac output. If the blood flow to the brain would be assumed to remain constant during (prolonged) locomotor activity, cases *Active1* and *Active2* should be ignored and *Rest2* would be the most extreme case. *Rest2* is exactly at the level where the recirculation started developing in this geometry. We conclude that it is challenging to estimate the effect of anesthesia and locomotor activity correctly, and that more research is needed to improve the accuracy of the corresponding boundary conditions.

ACKNOWLEDGMENTS

David De Wilde was supported by a research grant of the Flemish government agency for Innovation by Science and Technology (IWT, Grant number 111618). Bram Trachet is supported by a research grant of the Research Fund - Flanders (FWO, Grant number 12A5816N). We thank Christian Vanhove, Benedicte Descamps and Scharon Bruneel for their assistance with the in vivo experiments, Francisco Londono and Abigail Swillens for their assistance in processing the ultrasound measurements, Bert Vandeghinste for his assistance in processing the micro-CT scans and Mathias Peirlinck, Liesbeth Taelman, Joris Bols, Francesco Iannaccone,

Nic Debusschere, Joris Degroote and Jan Vierendeels for their assistance with the numerical simulations.

CONFLICT OF INTEREST STATEMENT

Currently, David De Wilde is working in the healthcare and manufacturing department of CGI Belgium.

REFERENCES

Asakura, T., Karino, T., 1990. Flow patterns and spatial distribution of atherosclerotic lesions in human coronary arteries. Circ. Res. 66, 1045-1066.

Assemat, P., Armitage, J.A., Siu, K.K., Contreras, K.G., Dart, A.M., Chin-Dusting, J.P., Hourigan, K., 2014. Three-dimensional numerical simulation of blood flow in mouse aortic arch around atherosclerotic plaques. Appl. Math. Model. 38, 4175-4185.

Bols, J., Taelman, L., De Santis, G., Degroote, J., Verhegghe, B., Segers, P., Vierendeels, J., 2016. Unstructured hexahedral mesh generation of complex vascular trees using a multi-block grid-based approach. Comput. Methods Biomech. Biomed. Eng. 19, 663-672.

Chatzizisis, Y.S., Coskun, A.U., Jonas, M., Edelman, E.R., Feldman, C.L., Stone, P.H., 2007. Role of Endothelial Shear Stress in the Natural History of Coronary Atherosclerosis and Vascular RemodelingMolecular, Cellular, and Vascular Behavior. J. Am. Coll. Cardiol. 49, 2379-2393.

Cheng, C., de Crom, R., van Haperen, R., Helderman, F., Gourabi, B.M., van Damme, L.C.A., Kirschbaum, S.W., Slager, C.J., van der Steen, A.F.W., Krams, R., 2004. The role of shear stress in atherosclerosis - Action through gene expression and inflammation? Cell Biochem. Biophys. 41, 279-294.

Cheng, C., Tempel, D., van Haperen, R., van der Baan, A., Grosveld, F., Daemen, M.J.A.P., Krams, R., de Crom, R., 2006. Atherosclerotic Lesion Size and Vulnerability Are Determined by Patterns of Fluid Shear Stress. Circulation 113, 2744-2753.

De Wilde, D., Trachet, B., Debusschere, N., Iannaccone, F., Swillens, A., Degroote, J., Vierendeels, J., De Meyer, G.R.Y., Segers, P., 2015a. Assessment of shear stress related parameters in the carotid bifurcation using mouse-specific FSI simulations. J. Biomech.

De Wilde, D., Trachet, B., Meyer, G.R.Y., Segers, P., 2015b. Shear Stress Metrics and Their Relation to Atherosclerosis: An In Vivo Follow-up Study in Atherosclerotic Mice. Ann. Biomed. Eng., 1-12.

Feintuch, A., Ruengsakulrach, P., Lin, A., Zhang, J., Zhou, Y.Q., Bishop, J., Davidson, L., Courtman, D., Foster, F.S., Steinman, D.A., Henkelman, R.M., Ethier, C.R., 2007. Hemodynamics in the mouse aortic arch as assessed by MRI, ultrasound, and numerical modeling. American Journal of Physiology-Heart and Circulatory Physiology 292, H884-H892.

Ford, M.D., Black, A.T., Cao, R.Y., Funk, C.D., Piomelli, U., 2011. Hemodynamics of the Mouse Abdominal Aortic Aneurysm. J. Biomech. Eng. 133.

Greve, J.M., Les, A.S., Tang, B.T., Blomme, M.T.D., Wilson, N.M., Dalman, R.L., Pelc, N.J., Taylor, C.A., 2006. Allometric scaling of wall shear stress from mice to humans: quantification using cine phase-contrast MRI and computational fluid dynamics. American Journal of Physiology-Heart and Circulatory Physiology 291, H1700-H1708.

Hiura, M., Nariai, T., Ishii, K., Sakata, M., Oda, K., Toyohara, J., Ishiwata, K., 2014. Changes in Cerebral Blood Flow during Steady-State Cycling Exercise: A Study Using Oxygen-15-Labeled Water with PET. J. Cereb. Blood Flow Metab. 34, 389-396.

Hoi, Y., Zhou, Y.-Q., Zhang, X., Henkelman, R., Steinman, D., 2011. Correlation Between Local Hemodynamics and Lesion Distribution in a Novel Aortic Regurgitation Murine Model of Atherosclerosis. Ann. Biomed. Eng. 39, 1414-1422.

Huo, Y.L., Guo, X.M., Kassab, G.S., 2008. The flow field along the entire length of mouse aorta and primary branches. Ann. Biomed. Eng. 36, 685-699.

Janssen, B.J.A., De Celle, T., Debets, J.J.M., Brouns, A.E., Callahan, M.F., Smith, T.L., 2004. Effects of anesthetics on systemic hemodynamics in mice. American Journal of Physiology - Heart and Circulatory Physiology 287, H1618-H1624.

Komarek, V., 2007. Normative biology, husbandry, and models - mouse physiology, The mouse in biomedical research II. Elsevier, pp. 23-90.

Ku, D.N., Giddens, D.P., Zarins, C.K., Glagov, S., 1985. Pulsatile flow and atherosclerosis in the human carotid bifurcation - positive correlation between plaque location and low and oscillating shear-stress. Arteriosclerosis 5, 293-302.

Marieb, E.N., Hoehn, K., 2008. Anatomy and Physiology. Pearson Benjamin Cummings.

Mohri, Z., Rowland, E.M., Clarke, L.A., De Luca, A., Peiffer, V., Krams, R., Sherwin, S.J., Weinberg, P.D., 2014. Elevated Uptake of Plasma Macromolecules by Regions of Arterial Wall Predisposed to Plaque Instability in a Mouse Model. PLoS ONE 9, e115728.

Nakashima, Y., Plump, A.S., Raines, E.W., Breslow, J.L., Ross, R., 1994. ApoE-deficient mice develop lesions of all phases of atherosclerosis throughout the arterial tree. Arterioscler. Thromb. Va c. Biol. 14, 133-140.

Peiffer, V., Bharath, A.A., Sherwin, S.J., Weinberg, P.D., 2013a. A Novel Method for Quantifying Spatial Correlations Between Patterns of Atherosclerosis and Hemodynamic Factors. J. Biomech. Eng. 135, 021023-021023.

Peiffer, V., Sherwin, S.J., Weinberg, P.D., 2013b. Does low and oscillatory wall shear stress correlate spatially with early atherosclerosis? A systematic review. Cardiovasc. Res. 99, 242-250.

Querido, J.S., Sheel, A.W., 2012. Regulation of Cerebral Blood Flow During Exercise. Sports Med. 37, 765-782.

Rowland, E.M., Mohamied, Y., Yean Chooi, K., Bailey, E.L., Weinberg, P.D., 2015. Comparison of Statistical Methods for Assessing Spatial Correlations Between Maps of Different Arterial Properties. J. Biomech. Eng. 137, 101003-101003.

Suo, J., Ferrara, D.E., Sorescu, D., Guldberg, R.E., Taylor, W.R., Giddens, D.P., 2007. Hemodynamic shear stresses in mouse aortas - Implications for atherogenesis. Arteriosclerosis Thrombosis and Vascular Biology 27, 346-351.

Trachet, B., Bols, J., De Santis, G., Vandenberghe, S., Loeys, B., Segers, P., 2011a. The Impact of Simplified Boundary Conditions and Aortic Arch Inclusion on CFD Simulations in the Mouse Aorta: A Comparison With Mouse-specific Reference Data. J. Biomech. Eng. 133, 121006-121013.

Trachet, B., Fraga-Silva, R.A., Piersigilli, A., Segers, P., Stergiopulos, N., 2015. Dissecting abdominal aortic aneurysm in ang II-infused mice: the importance of imaging. Curr. Pharm. Des. 21, 4049-4060.

Trachet, B., Renard, M., De Santis, G., Staelens, S., De Backer, J., Antiga, L., Loeys, B., Segers, P., 2011b. An integrated framework to quantitatively link mouse-specific hemodynamics to aneurysm formation in angiotensin II-infused ApoE -/- mice. Ann. Biomed. Eng. 39, 2430-2444.

Trachet, B., Swillens, A., Van Loo, D., Casteleyn, C., De Paepe, A., Loeys, B., Segers, P., 2009. The influence of aortic dimensions on calculated wall shear stress in the mouse aortic arch. Comput. Methods Biomech. Biomed. Eng. 12, 491-499.

Van Doormaal, M., Zhou, Y.-Q., Zhang, X., Steinman, D.A., Mark Henkelman, R., 2014. Inputs for Subject-Specific Computational Fluid Dynamics Simulation of Blood Flow in the Mouse Aorta. J. Biomech. Eng. 136, 101008-101008.

Willett, N.J., Long, R.C., Maiellaro-Rafferty, K., Sutliff, R.L., Shafer, R., Oshinski, J.N., Giddens, D.P., Guldberg, R.E., Taylor, W.R., 2010. An In Vivo Murine Model of Low-Magnitude Oscillatory Wall Shear Stress to Address the Molecular Mechanisms of Mechanotransduction—Brief Report. Arterioscler. Thromb. Va c. Biol. 30, 2099-2102.

Yap, C.H., Liu, X., Pekkan, K., 2014. Characterizaton of the Vessel Geometry, Flow Mechanics and Wall Shear Stress in the Great Arteries of Wildtype Prenatal Mouse. PLoS ONE 9, e86878.

TABLES

Scale factor/ Condition	Q	P_{sys} (mmHg)	P_{dia} (mmHg)	T (s)	HR (beats/min)
Anesthesia	1.00	119	87	0.1719	349
Rest1	1.06	119	87	0.1530	392
Rest2	1.72	119	87	0.1066	563
Active1	2.04	156	114	0.1236	485
Active2	3.33	156	114	0.0861	697

Table 1. Adaptation of the boundary conditions to account for anesthesia and locomotor activity.

FIGURE LEGENDS

Figure 1. Imposed flow profiles for transient CFD (a) and FSI (b) simulations, and resulting cross-sectional areas (c) at the in-and outlets of the model.

Figure 2. (a) Correlation between the TAWSS as calculated by FSI (assuming anesthesia) and the (TA)WSS calculated by mean, peak and transient CFD. (b) Correlation between the OSI as calculated by FSI (assuming anesthesia) and the OSI calculated by transient CFD. (c) Correlation between the TAWSS calculated assuming anesthesia and the TAWSS calculated assuming different locomotor activity levels. Remark that the Y-axis is not on the same scale, as the absolute value of TAWSS increased with increasing activity (and flow). (d) Correlation between the OSI calculated assuming anesthesia and the OSI calculated assuming different locomotor activity levels. *: $p<0.05$, **: $p<0.001$; ns: not significant.

Figure 3. Qualitative comparison of the influence of computational techniques (assuming anesthesia) for TAWSS (a), normalized TAWSS (b) and OSI (c).

Figure 4. Qualitative comparison of the influence of anesthesia and locomotor activity (using FSI simulations) on TAWSS (a), normalized TAWSS (b), OSI (c). In panel d the reversed WSS area is quantified for all techniques and all physiological conditions. The close-up shows the transient CFD simulation with both reversed WSS zones: stagnation point (blue) and the outer sinus of the ECA (red).

Figure 5. The line integral convolution (LIC) shows recirculation zones in the WSS at the anterior side of the ECA (a) and in the mid-plane of the ECA (b). The LIC is plotted at the early deceleration phase for different activity states (a), and at different time points for the *Active2* case (b).

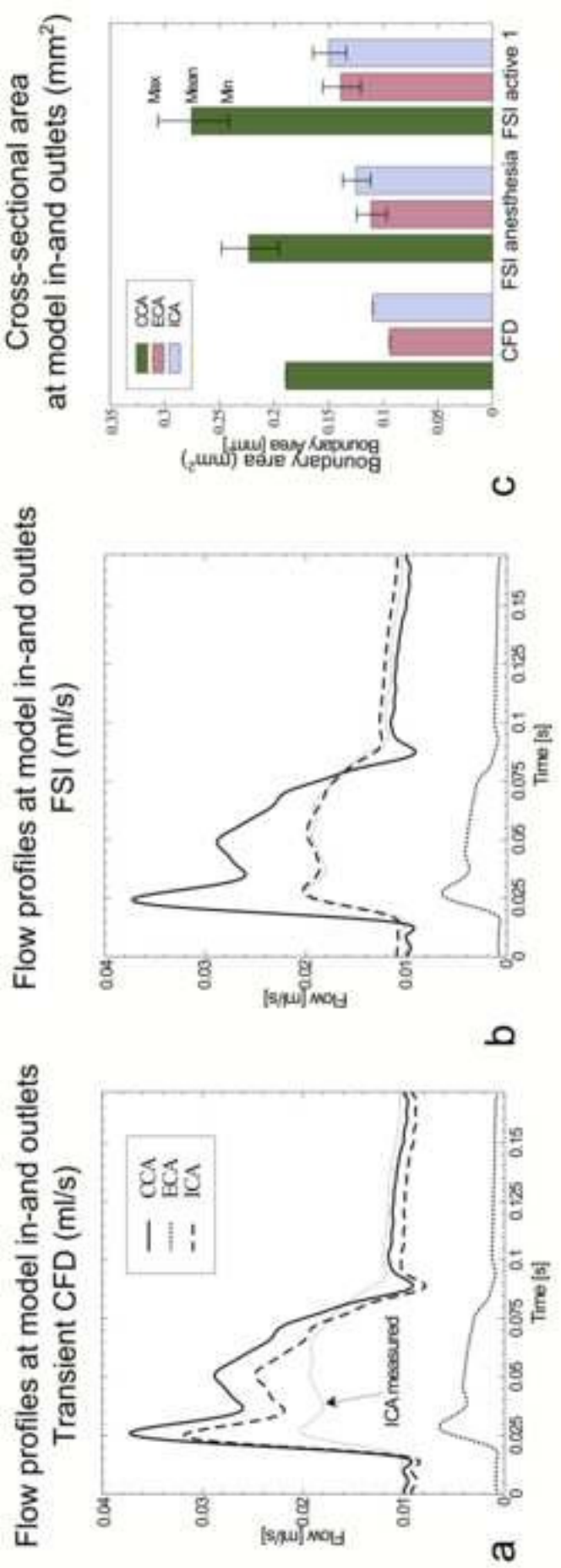

Figure 1

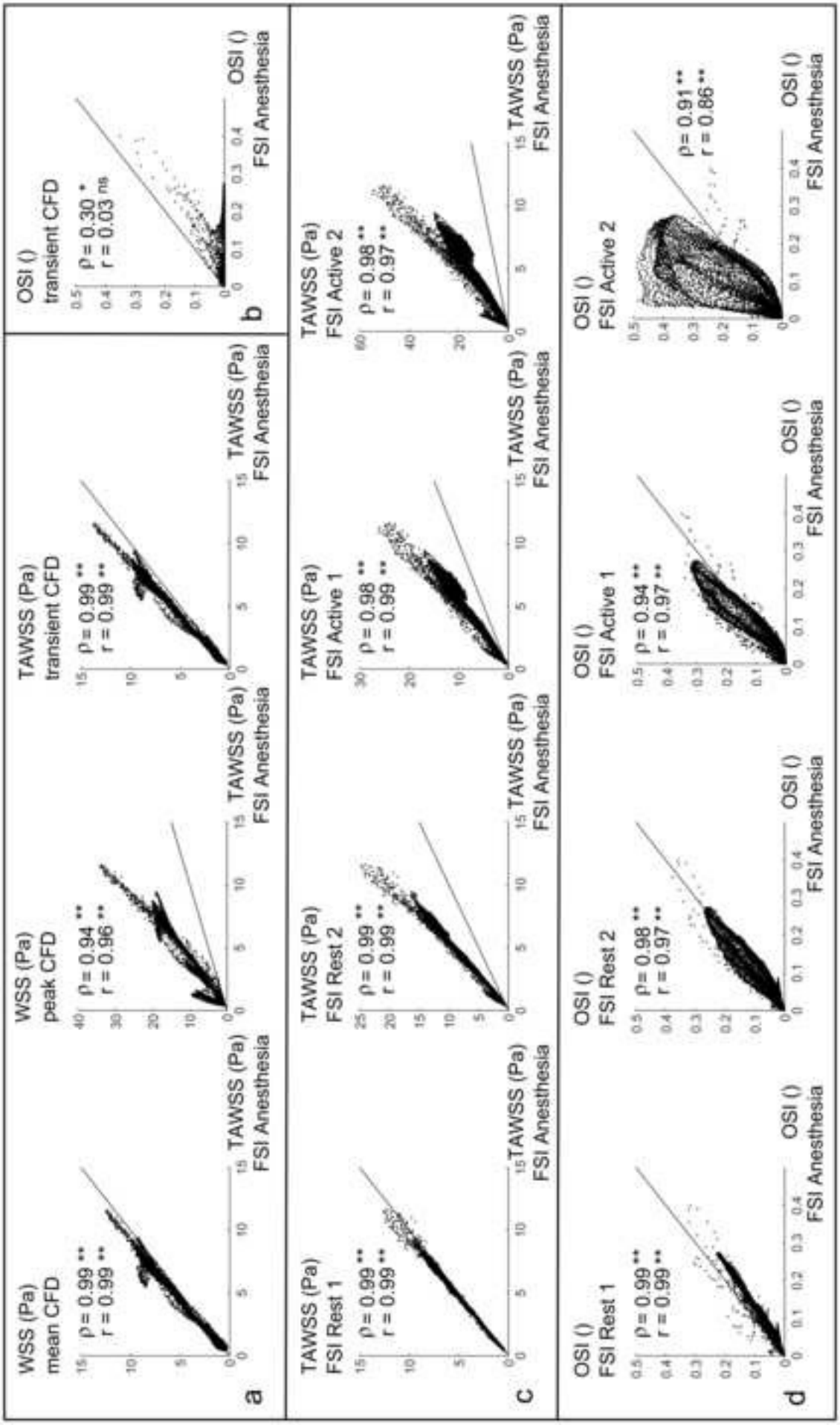
a
WSS (Pa)
mean CFD
ρ= 0.99 **
r = 0.99 **
TAWSS (Pa)
FSI Anesthesia
WSS (Pa)
peak CFD
ρ= 0.94 **
r = 0.96 **
TAWSS (Pa)
FSI Anesthesia
TAWSS (Pa)
transient CFD
ρ= 0.99 **
r = 0.99 **
TAWSS (Pa)
FSI Anesthesia
b
OSI ()
transient CFD
ρ= 0.30 *
r = 0.03 ns
OSI ()
FSI Anesthesia
c
TAWSS (Pa)
FSI Rest 1
ρ= 0.99 **
r = 0.99 **
TAWSS (Pa)
FSI Anesthesia
TAWSS (Pa)
FSI Rest 2
ρ= 0.99 **
r = 0.99 **
TAWSS (Pa)
FSI Anesthesia
TAWSS (Pa)
FSI Active 1
ρ= 0.98 **
r = 0.99 **
TAWSS (Pa)
FSI Anesthesia
TAWSS (Pa)
FSI Active 2
ρ= 0.98 **
r = 0.97 **
TAWSS (Pa)
FSI Anesthesia
d
OSI ()
FSI Rest 1
ρ= 0.99 **
r = 0.99 **
OSI ()
FSI Anesthesia
OSI ()
FSI Rest 2
ρ= 0.98 **
r = 0.97 **
OSI ()
FSI Anesthesia
OSI ()
FSI Active 1
ρ= 0.94 **
r = 0.97 **
OSI ()
FSI Anesthesia
OSI ()
FSI Active 2
ρ= 0.91 **
r = 0.86 **
OSI ()
FSI Anesthesia

Figure 2

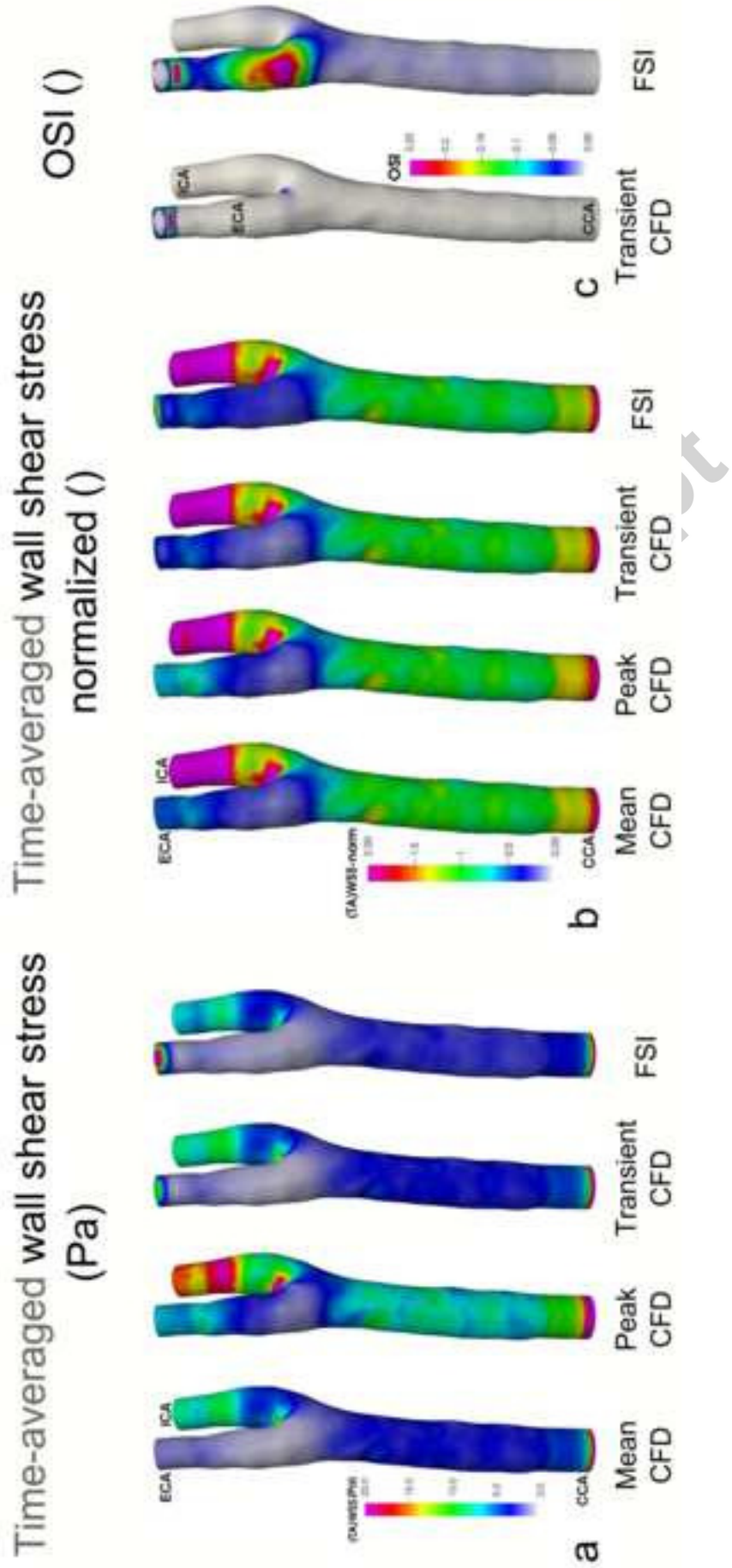
Time-averaged wall shear stress (Pa)
Time-averaged wall shear stress normalized ()
OSI ()
Mean CFD
Peak CFD
Transient CFD
FSI
ECA
ICA
CCA
a
b
c

Figure 3

Figure 4

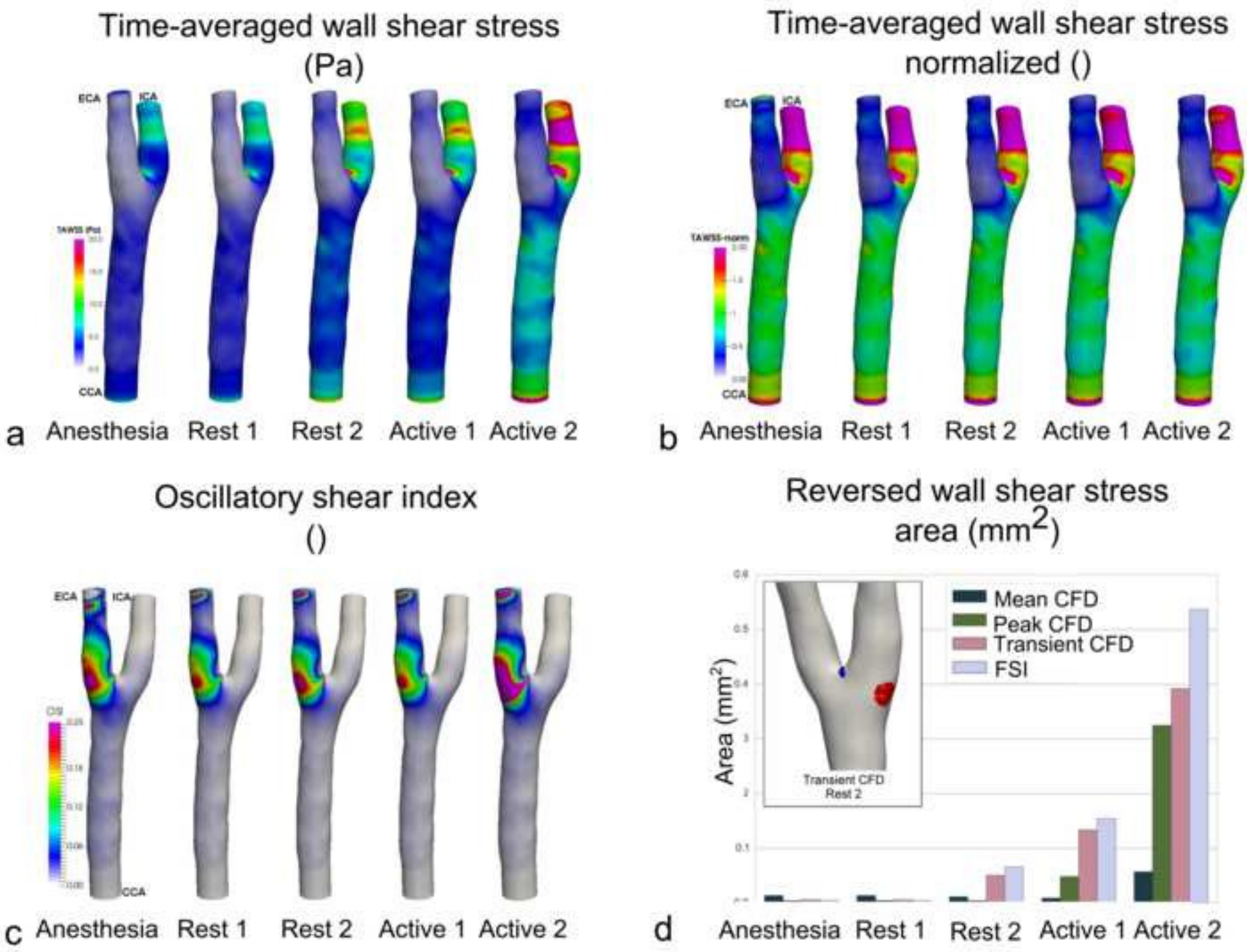

Figure 5